



Employing airborne radiation and cloud microphysics observations to improve cloud representation in ICON at kilometer-scale resolution in the Arctic

Jan Kretzschmar¹, Johannes Stapf¹, Daniel Klocke^{2,3}, Manfred Wendisch¹, and Johannes Quaas¹

¹Institute for Meteorology, Universität Leipzig, Leipzig, Germany

²Deutscher Wetterdienst, Offenbach, Germany

³Hans-Ertel-Zentrum für Wetterforschung, Offenbach, Germany

Correspondence: Jan Kretzschmar (jan.kretzschmar@uni-leipzig.de)

Abstract. Clouds play a potentially important role in Arctic climate change, but are poorly represented in current atmospheric models across scales. To improve the representation of Arctic clouds in models, it is necessary to compare models to observations to consequently reduce this uncertainty. This study compares aircraft observations from the Arctic Cloud Observations Using Airborne Measurements during Polar Day (ACLOUD) campaign in May/June 2017 around Svalbard, Norway - to simulations using the ICON (ICOsahedral Non-hydrostatic) model in its numerical weather prediction (NWP) set-up at 1.2 km resolution. By comparing measurements of solar and terrestrial irradiances during ACLOUD flights to the respective properties in ICON, we showed that the model systematically overestimates the transmissivity of the mostly liquid clouds during the campaign. This model bias is traced back to the way cloud condensation nuclei (CCN) get activated into cloud droplets in the two-moment, bulk microphysical scheme used in this study. This process is parameterized as function of grid-scale vertical velocity in the microphysical scheme used, but in-cloud turbulence cannot sufficiently be resolved at 1.2 km horizontal resolution in Arctic clouds. By parameterizing subgrid-scale vertical motion as a function of turbulent kinetic energy, we are able to achieve a more realistic CCN activation into cloud droplets. Additionally, we showed that by scaling the presently used CCN activation profile, the hydrometeor number concentration could be modified to be in better agreement with ACLOUD observations in our revised CCN activation parameterization. This consequently results in an improved representation of cloud optical properties in our ICON simulations.

1 Introduction

In recent decades, the Arctic has proven to be especially susceptible to global climate change (Screen and Simmonds, 2010), as several positive feedback mechanisms strengthen the warming in high latitudes of the Northern Hemisphere (Serreze and Barry, 2011). Among those feedback mechanisms that influence the Arctic climate, the cloud feedback - even though being small in



magnitude compared to other feedback mechanisms like the surface albedo or temperature feedbacks - exhibits a relatively large uncertainty (Pithan and Mauritsen, 2014; Block et al., 2020). This uncertainty can be related to the general complexity of the Arctic climate system and to misrepresented microphysical processes in global climate models (GCMs) that are used to quantify the cloud feedback. Typical issues associated with the simulation of clouds in the Arctic are incorrectly simulated amount and distribution of clouds (English et al., 2015; Boeke and Taylor, 2016), which often can be linked to an erroneous representation of mixed-phase clouds (Cesana et al., 2012; Pithan et al., 2014; Kretzschmar et al., 2019). This consequently affects the quantification of the effect of Arctic clouds on the (surface) energy budget in GCMs (Karlsson and Svensson, 2013). To identify processes within the microphysical parametrization that are misrepresented in models, it is inevitable to compare them to observations (Lohmann et al., 2007). As pointed out by Kay et al. (2016), any comparison between modeled and observed quantities can easily be misleading if it is not scale- and definition-aware. For GCMs, observations from satellite remote sensing are well suited, being on similar scales as those large scale models. A comparison to satellite derived quantities can further be made definition-aware by using instrument simulators like they are provided within the Cloud Feedback Model Intercomparison Project's (CFMIP) Observation Simulator Package (COSP; Bodas-Salcedo et al., 2011). The benefit of using COSP for evaluating clouds in GCMs in the Arctic has been shown in several studies (Barton et al., 2012; Kay et al., 2016; Kretzschmar et al., 2019).

Even though satellite observations provide valuable information on the atmospheric state in the Arctic, they often suffer from instrument dependent idiosyncrasies like ground clutter for a space-borne cloud radar or attenuation of the beam of a space-borne lidar by optical thick clouds (Cesana et al., 2012). Those problems can be in part overcome by using ground-based or aircraft observations. Due to much smaller temporal and spatial scales, those observations only have limited suitability for the evaluation of large-scale models. To this end, the use of storm-resolving models with grid sizes on the order of kilometers or large eddy models is necessary, as they are able to better capture features and variability present in those rather smaller scale observations (Stevens et al., 2019). Due to the relatively large computational effort that is needed for large eddy simulations, they are limited in spatial extent and, for that reason, are often used for comparison with ground based observations at individual locations in the Arctic (Loewe et al., 2017; Sotiropoulou et al., 2018; Neggers et al., 2019; Schemann and Ebell, 2020). If one wants to use aircraft observations of the Arctic atmosphere to compare it to models, the computational resources needed for such a comparison can be a limiting factor to perform such highly resolved simulation, especially when multiple days should be considered. Nevertheless, a comparison of large eddy simulations to aircraft observations for well-defined situations can give valuable insights into physical processes within the Arctic atmosphere. Such simulations can be particularly useful when the high resolution of a large eddy set-up is explicitly needed to allow for a comparison with small scale phenomena like in-cloud turbulence (Mech et al., 2020) or cloud-top inhomogeneity (Schäfer et al., 2018; Ruiz-Donoso et al., 2020) that are observed from the airborne remote sensing. To avoid the need for large computational resources but still be able to resolve many processes that act on scales that cannot be captured by GCMs, limited area simulations with grid sizes on the order of a few kilometers where (deep) convection does not need to be explicitly parameterized can offer a good compromise. Simulations at such resolutions on relatively large domains have received increased interest in recent years (Stevens et al., 2019).

This study makes use of such a set-up using the ICOSahedral Non-hydrostatic (ICON) model (Zängl et al., 2015) at kilometer-



scale horizontal resolution. Studies, mainly focusing on the tropical Atlantic, have shown that the model at storm-resolving resolutions is able to simulate the basic structure of clouds and precipitation in that region (Klocke et al., 2017; Stevens et al., 2020). In the present study, ICON is used in a similar set-up and is compared to observations that have been derived from the Arctic Cloud Observations Using Airborne Measurements during Polar Day (ACLOUD) campaign in May/June 2017 around Svalbard, Norway (Wendisch et al., 2019; Ehrlich et al., 2019). This study compares observations of solar and terrestrial irradiances during ACLOUD flights to our ICON simulations to obtain a first estimate whether the model is able to correctly simulate general cloud optical properties. Based on the results of this comparison, it is further explored to what extent cloud macro- and microphysical properties might be misrepresented in this set-up and how to improve the simulation of clouds in ICON at kilometer-scale.

2 Data and model

2.1 ACLOUD/PASCAL campaign

In May and June 2017, two concerted field studies took place around Svalbard, Norway (Wendisch et al., 2019): the Arctic Cloud Observations Using Airborne Measurements during Polar Day (ACLOUD; Ehrlich et al., 2019) campaign and the Physical Feedbacks of Arctic Boundary Layer, Sea Ice, Cloud and Aerosol (PASCAL; Flores and Macke, 2018) ship-borne observational study. The airborne measurements during ACLOUD were conducted with the two research aircraft Polar 5 and Polar 6 (Wesche et al., 2016) that were based in Longyearbyen (LYR), Norway. While Polar 5 focused on remote sensing observations of mainly low-level clouds and surface properties from higher altitudes (2-4 km), Polar 6 concentrated on in situ observations of cloud microphysical and aerosol properties, in and below the clouds. Ground-based observations from the ship and an ice floe in the sea ice covered ocean north of Svalbard were performed during PASCAL using the German research vessel (R/V) Polarstern (Knust, 2017). Additionally, a tethered balloon was operated on an ice floe camp during PASCAL (Egerer et al., 2019).

The synoptic development during both campaigns is separated into three phases (Knudsen et al., 2018). A period with advection of cold and dry air from the north in the beginning (23-29 May 2017) was followed by a warm and moist air intrusion into the region where the two campaigns took place (30 May -12 June 2017). During the final two weeks of the campaigns (13-26 June 2017), a mixture of warm and cold airmasses prevailed. Especially during the last two phases, clouds in the domain close to Polarstern, where the bulk of the measurements took place, mainly consisted of (super-cooled) liquid clouds with only little cloud ice being present (Wendisch et al., 2019).

In the following, a brief description of the instrumentation and data used in this study is given (for a comprehensive overview we refer Wendisch et al. (2019) and Ehrlich et al. (2019)). Two pairs of upward and downward looking CMP 22 pyranometers for the solar (0.2-3.6 μm) and CGR4 pyrgeometers for major parts of the terrestrial spectral range (4.5-42 μm) were installed on board of Polar 5 and Polar 6 to measure the upward and downward broadband (solar and terrestrial) irradiances on both aircraft (Stapf et al., 2019b). We also utilize microphysical data that have been derived from in-situ measurements on Polar 6. We use data of the particle size number distribution obtained from the Small Ice Detector Mark 3 (SID-3) (Schnaiter and Järvinen,

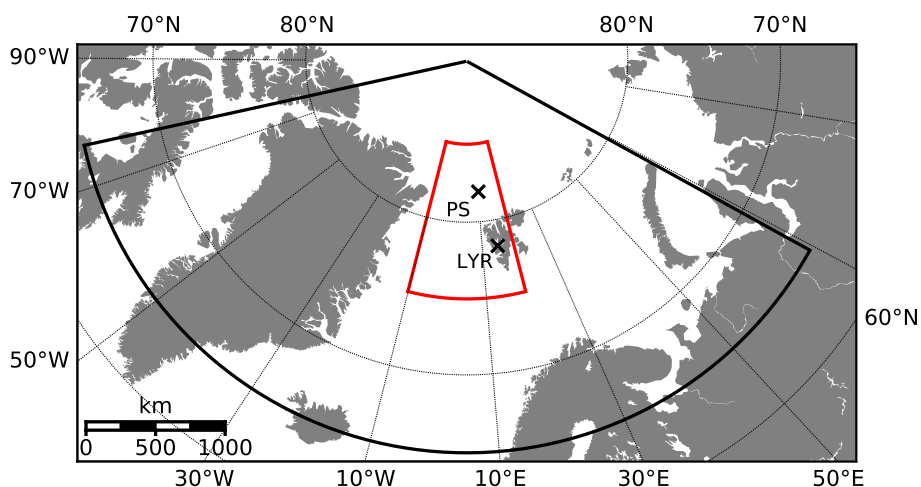


Figure 1. Set-up of the limited-area simulations. The outer domain (black) has an approximate resolution of 2.4 km, while the inner domain has a resolution of 1.2 km. Additionally marked is Longyearbyen/Norway (LYR) where Polar 5 and Polar 6 were stationed during ACLOUD, as well as the position of the R/V Polarstern (PS) during the ice floe camp.

2019) covering a size range of 5–45 μm divided into 16 size bins (2–5 μm resolution). For more information on the SID-3 and processing of the measurements, the reader is referred to Schnaiter et al. (2016) and Ehrlich et al. (2019). For comparison of the bulk liquid water content, we exploit data from a Nevzorov probe (Korolev et al., 1998) that was installed on Polar 6 (Chechin, 2019).

2.2 ICON simulations

In this study, data measured during ACLOUD and PASCAL is compared to the output of the ICOSahedral Non-hydrostatic model (ICON; Zängl et al., 2015). ICON is a unified modelling systems that allows simulations on several spatial and temporal scales, spanning from simulation of the global climate on the one end (Giorgetta et al., 2018) to high resolution large eddy simulations (LES) on the other (Dipankar et al., 2015; Heinze et al., 2017). ICON is also employed as a numerical weather prediction (NWP) model at the German Meteorological Service (Deutscher Wetterdienst, DWD). For each application (GCM, NWP, LES), a dedicated package of physical parametrizations is provided to satisfy the specific needs for each set-up. For our simulations, the applied set of physical parametrizations is similar to that used in Klocke et al. (2017). However, we use the two-moment, bulk microphysical scheme developed by Seifert and Beheng (2006) instead of the single moment scheme by Baldauf et al. (2011) used in Klocke et al. (2017). Furthermore, we apply an all-or-nothing cloud cover scheme that allows for grid-scale clouds only. The Rapid Radiation Transfer Model (RRTM; Mlawer et al., 1997) is applied to derive the radiative fluxes. Due to the rather fine horizontal resolution of our simulations, we only parametrized shallow convection using the Tiedtke (1989) shallow convection parameterization with modifications by Bechtold et al. (2008), whereas deep convection is considered resolved (albeit not relevant for the Arctic case considered here). In the following, the used set-up will be simply



denoted as ICON. However, findings in this study are specific to our chosen set-up (spatial scale and parameterizations used) and should not be seen as general feature of ICON.

We deploy ICON in a limited-area set-up with one local refinement (nest) in the region where the research flights and ship observations were performed (Figure 1). The outer domain has a horizontal resolution of approximately 2.4 km (R2B10 in the triangular refinement) while the inner nest has a refined resolution (R2B11) of approximately 1.2 km. For both domains, we use 75 vertical levels spanning from the surface to 30 km altitude with a vertical resolution of 20 m at the lowest model level that gradually gets coarser towards model top. We initialize the model using the analysis of European Center of Medium Weather Forecast (ECMWF) Integrated Forecasting System (IFS). The respective IFS forecast is used as boundary data to which we nudge our model every three hours. We do not continuously run the model for the whole period of the campaign but re-initialize the model from the 1200 UTC analysis of the previous day in case of a subsequent day with flight activities. This gives the model a spin-up time of more than 12 hours even for takeoffs in the early morning.

During the initial comparison of ICON and the ACLOUD observations, we found that the albedo of sea ice in the model is substantially lower compared to values observed during ACLOUD (Wendisch et al., 2019). The reason for this underestimation of the surface albedo in ICON is caused by the way how our simulations are initialized using the IFS analysis. As the IFS sea ice albedo is not used during the initialization of ICON, the parametrization of the sea ice albedo performs a cold start. For such a cold start, the sea ice albedo is only a function of the sea ice surface temperature as given by Mironov et al. (2012) (their Equation 5). This formulation was slightly adapted in ICON by setting the maximum sea ice albedo (α_{\max}) to 0.70 and the minimum sea ice albedo (α_{\min}) to 0.48. For surface temperatures close the freezing point (as it has been observed during ACLOUD, especially in the second half of the campaign), such a cold start results in albedo values that are considerably lower compared to the observations. This underestimation of the sea ice albedo could be avoided by increasing the spin-up of the model to a few weeks or by using DWD ICON analysis instead of the IFS analysis. In the latter case, the albedo is initialized from the initial data and no spin-up is required (Wendisch et al., 2019). As one of the main aims of this comparison are radiative fluxes, an accurate representation of surface albedo is crucial and we, therefore, chose to take yet another approach. For each day, we use prescribed values for the sea ice albedo that are derived from the aircraft observations. For this purpose, from the observations, only scenes with homogeneous sea ice are selected using a fish-eye-camera-derived sea ice concentration threshold of 95 %. The daily averaged observed albedo is parameterized as a function of day of the year and is held constant for any specific day. This approach by construction results in a standard deviation of as little as 0.024 between modeled and observed albedo. In case of fractional sea ice cover in the model, the surface albedo is a surface fraction-weighted average between the prescribed value and the albedo of open water (taken as 0.07).

For the comparison of our ICON simulations to the ACLOUD data, we temporally and spatially collocate the model output to be consistent with the actual position and altitude of the aircraft. We use a multidimensional binary search tree (also known as k-d tree; Bentley, 1975) to sample the model output along the flight track in space and time directly on its native unstructured, triangular grid. The temporal frequency of the observational data is 1 Hz. Additionally, we averaged the (sampled) datapoints from the observations and the simulations into 20 second intervals. This ensures that the observational data is on a similar spatial scale as the simulation on the 1.2 km grid of the inner domain (considering an average velocity of the aircraft of 60 m s^{-1}).

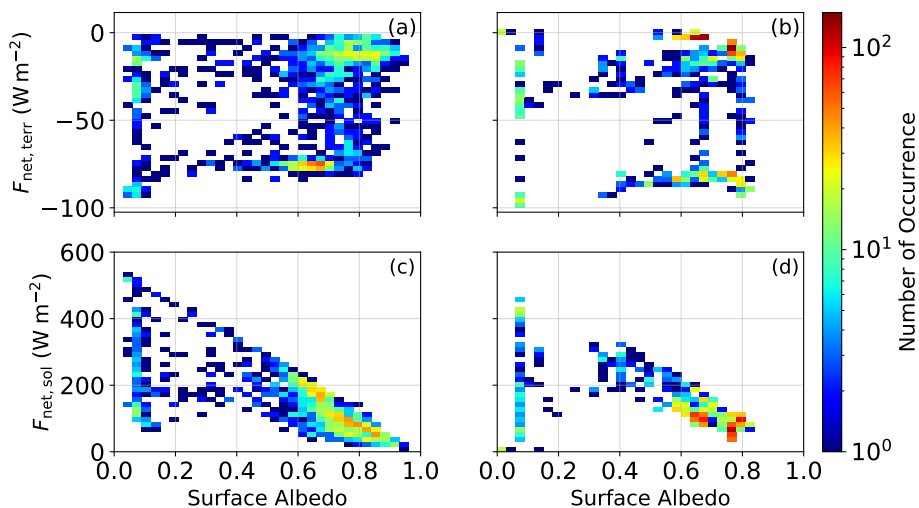


Figure 2. Two dimensional histograms of surface albedo and (top row; a, b) net terrestrial-/ (bottom row; c, d) net solar irradiance at the surface (W m^{-2}) for (left column; a, c) ACloud observations and (right column; b, d) ICON simulations.

Due to storage constraints, we chose to output the model state only every 30 minutes, which reduces temporal variability in the model output. As the planes are not static and "fly" through the model grid, temporal variability is, to some extent, replaced by spatial variability when sampling a large enough area along the flight track. Additionally, the 30 minute output frequency introduces inconsistencies in the top of atmosphere incoming solar irradiance as the solar zenith angle is constant in the model output while it varies with time in the observations within those 30 minute intervals. Even though being on similar scales, spatial and temporal variability in both datasets prohibit a one-to-one comparison. We will, therefore, mainly use histograms in the comparison.

3 Surface radiative quantities as simulated with ICON and measured during ACloud

In the following, the simulations are compared to data for several surface radiative variables that have been observed during low-level flight sections. Some flights were excluded due to relatively short flight times to save computational resources. Additionally, some flights with cloudless conditions towards the end of the campaign were excluded as the main focus of this study is a comparison of cloud properties. An overview of the flights used for the comparison is given in Table 1. In the observation and in the model, we define low-level flight sections as such that no cloud is present below the present altitude of the aircraft.

3.1 Spatial structure of the radiative field of the Arctic atmospheric boundary layer

In the Arctic, two distinct radiative states have been reported: a radiatively clear state with no, or only radiatively thin clouds and a cloudy state with opaque clouds (Shupe and Intrieri, 2004; Stramler et al., 2011). This two-state structure was also



Table 1. Flights used for the comparison to ICON simulations. The values given for the low-level scenes corresponds to the number of the averaged 20 second intervals used in the following comparison. For more information on the scientific target of each research flight, refer to Wendisch et al. (2019) and Ehrlich et al. (2019).

Flight No.	Date in 2017	Flight Time (UTC)		Low-level scenes	
		Polar 5	Polar 6	all-sky + all surfaces	cloudy + sea ice
4	23 May	09:12-14:25	-	69	12
5	25 May	08:18-12:46	-	-	-
6	27 May	07:58-11:26	-	-	-
7	27 May	13:05-16:23	13:02-16:27	58	-
8	29 May	04:54-07:51	05:11-09:17	60	-
10	31 May	15:05-18:57	14:59-19:03	199	-
11	2 June	08:13-13:55	08:27-14:09	73	7
12	4 June	-	10:06-15:39	65	55
13	5 June	10:48-14:59	10:43-14:44	101	70
14	8 June	07:36-12:51	07:30-13:20	80	6
17	14 June	12:48-18:50	12:54-17:37	275	275
18	16 June	04:45-10:01	04:40-10:31	-	-
19	17 June	09:55-15:25	10:10-15:55	95	22
20	18 June	12:03-17:55	12:25-17:50	131	-
23	25 June	11:09-17:11	11:03-16:56	347	-

observed during ALOUD, but compared to spatially fixed observations with almost constant surface albedo, observations during ALOUD were further decomposed into a cloudy and cloudless state over sea ice and open ocean, which consequently results in a four-state structure (Wendisch et al., 2019). As in Wendisch et al. (2019), we compiled two-dimensional histograms of surface albedo and surface net terrestrial/net solar irradiance, which is defined as the difference between downward and upward radiative energy flux densities, for the ALOUD observations and the ICON simulations (Figure 2). The general difference to Wendisch et al. (2019) (their Figure 14) is explained by the prescribed surface albedo approach applied in this study, which results in higher sea ice albedo values compared to the previous comparison.

In general, the structure of the modeled net terrestrial irradiance ($F_{\text{net,terr}}$) close to the surface (Figure 2 a/b) is in agreement with the observed one. Only for surface albedo values between 0.6 and 0.7, differences between the ALOUD observations and the

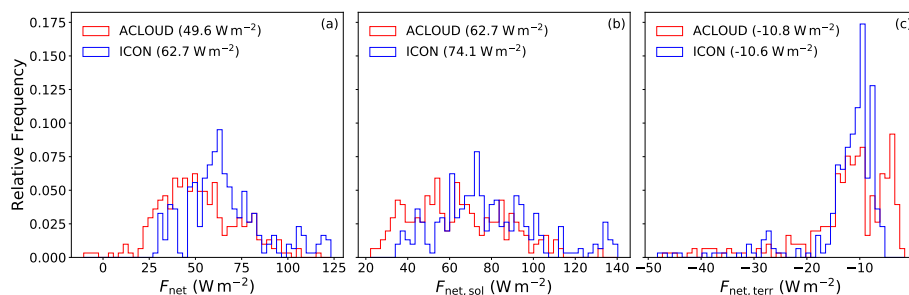


Figure 3. Relative frequency distributions of (blue) modeled and (red) observed surface net irradiation for sea-ice covered surfaces and cloudy conditions for (a) total radiation, (b) solar, and (c) terrestrial radiation. Values in the legend indicate the median of the respective variables.

ICON simulations become obvious. Those albedo values are related to days towards the end of the campaign (mid/late June 2017) when the melting season had begun and sea ice albedo was reduced. For this period, the model overestimates the presence
170 of cloudy conditions whereas cloudless conditions were present in the ACloud observations. Conversely, for situations with sea ice albedo greater than 0.7, ICON overestimates the presences of cloudless conditions. The lack of cloudless conditions for surface albedo values between 0.6 and 0.7 in the ICON simulations is also visible from the histograms of surface albedo and net solar irradiance (Figure 2 c/d). For surface albedo larger than 0.7, the net solar irradiance ($F_{\text{net,sol}}$) close to the surface seems, on average, to be in agreement with the observations, even though the observed variability in surface albedo is not simulated
175 by the model. The reported discrepancies can be influenced by the input used to force our limited-area simulations. This can be seen in the underestimation of the albedo of sea ice covered surface despite the prescribed surface albedo in the model that is in accordance with the observed sea ice albedo. This bias is, therefore, related to differences in sea ice fraction in the model and in the observation and indicates that the sea ice fraction in the ECMWF input data is too small.

3.2 Surface net irradiances and cloud radiative effect over sea ice and below clouds

180 This section explores the effect of clouds on the surface radiative budget in the ACloud observations and in our ICON simulations over sea ice. For that purpose, we, at first, look at net surface irradiance, which we further split into its solar and terrestrial components. To ensure comparability despite obvious differences between the ICON simulations and ACloud observations described in subsection 3.1, we will restrict our comparison to situations where the model and the observations are within the same cluster of the two-dimensional histograms of surface albedo and surface net terrestrial irradiance at the
185 same time. To distinguish between those clusters, a situation is defined as cloudy if the net terrestrial irradiance at the surface is larger than -50 W m^2 and a surface is classified sea ice covered, if the surface albedo is larger than 0.5. As we are interested in cloud (radiative) properties over sea ice covered surface, we will focus our evaluation on those situations. Furthermore, this cluster is appealing as most low-level flight sections were performed under these conditions.

In Figure 3, we compare observed and simulated net near surface irradiances using histograms. From Figure 3 a, it becomes
190 obvious that the model systematically overestimates net surface irradiances below clouds and over sea ice. This variable also



shows a quite strong variability for both the model and the observations, which is related to varying sea ice albedo during the campaign. Additionally, the incoming solar radiation varied between research flights as they took place at different times of the day, which also introduces further variability. Looking at medians of the spectral components, we find that differences between simulated and observed net surface irradiances are mainly mediated by its solar component, while the median of net terrestrial surface irradiances are well simulated by ICON and also the shape of their histograms match better. Besides the above reported underestimated surface albedo for sea ice covered surface in ICON, also misrepresented cloud optical properties can contribute to the positive bias in net solar irradiances at the surface.

Furthermore, we investigate the surface cloud radiative effect (CRE) during ACLOUD, which is defined as the difference between net surface irradiance for cloudy and cloudless conditions. In the model, cloudy and cloudless irradiances can easily be derived by a double call to the radiation routines, one with clouds and one without clouds leaving all variables not related to clouds constant. For observations, it is impossible to simultaneously observe both cloudy and cloudless conditions. Therefore, irradiances of cloudless conditions were obtained from dedicated radiative transfer simulations based on measurements of atmospheric/surface observations (Stapf et al., 2019a). While the prescribed functional dependence of the sea ice albedo has been derived for cloudless and cloudy conditions, the surface albedo that is used to derive the CRE from the observations is for cloudy-sky only. This can lead to inconsistencies between the modeled and observed CRE (Stapf et al., 2019a).

The overwhelming majority of the observed and modeled total (solar plus terrestrial) surface CRE values are positive over sea ice, which indicates that clouds have a warming effect on the surface (Figure 4a). This is consistent with the relatively high surface albedo values at the onset of the melting period during ACLOUD (Jäkel et al., 2019; Wendisch et al., 2019), which decreases the cooling effect of clouds in the solar spectral range. Similar to the net surface irradiance, ICON overestimates the total surface CRE (Figure 4a), which is mainly caused by less cooling due to solar CRE (Figure 4b), while the modeled terrestrial CRE again matches the observed surface terrestrial CRE (Figure 4c). The way how the surface solar CRE is defined allows to narrow down, which effect is the main cause for the overestimated net solar surface irradiances. If clouds would be perfectly simulated by the model, the negatively biased surface albedo would cause a too strongly negative surface solar CRE. As this is not the case for ICON, it is inferred that the main cause for the overestimated net solar surface irradiances is related to overestimated transmissivity of the cloud layer, which is defined as the fraction of downward transmitted solar irradiance at cloud base to downward incident solar irradiance at cloud top. Therefore, underestimated cooling effects in the solar spectral range are most likely related to incorrect simulations of microphysical or macrophysical properties of Arctic clouds in ICON. In the following section, we therefore compare those properties as they were simulated (ICON) and measured (ACLOUD) in more detail.

220 4 Comparison of macro- and microphysical cloud properties in ICON to ACLOUD observations

Transmissivity T of a cloud layer is directly related to its optical thickness τ_c :

$$T = \exp(-\tau_c), \quad (1)$$

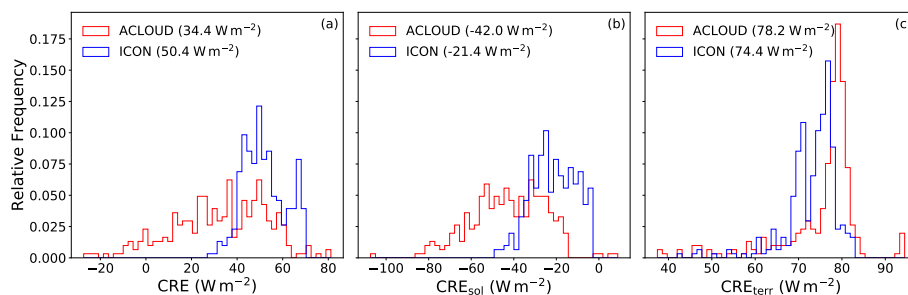


Figure 4. As Figure 3, but for the (a) total, (b) solar, and (c) terrestrial net cloud radiative effect at the surface.

where τ_c is defined as the vertical integral of the volumetric cloud extinction coefficient β_{ext} from cloud base z_{base} to cloud top z_{top} :

$$225 \quad \tau_c = \int_{z_{\text{base}}}^{z_{\text{top}}} \beta_{\text{ext}}(z) dz. \quad (2)$$

During ACLOUD and PASCAL, clouds were mostly in the liquid water phase with only little ice present, which allows to express the extinction coefficient as a function of liquid water content q_c and cloud droplet number concentration N_d (Grosvenor et al., 2018):

$$\beta_{\text{ext}} \sim N_d^{\frac{1}{3}} \cdot q_c^{\frac{2}{3}}. \quad (3)$$

230 Equation 3 and Equation 2 show that τ_c depends on macrophysical (geometrical depth, $z_{\text{top}} - z_{\text{base}}$) and microphysical properties (i.e., N_d and q_c) of the cloud layer.

To identify potential sources explaining the model-measurement differences discussed in the previous section, we compare geometrical thickness and microphysical properties of clouds in ICON to observations collected during ACLOUD/PASCAL. We decided to focus on the period from 2 June to 5 June 2017 when flights were possible on three out of four days. This period
 235 is favored because only low-level, mostly single layer clouds were present, which simplifies interpretation. During this period, a southerly to easterly inflow of warm and moist air into the region where research flights took place was observed (Knudsen et al., 2018).

4.1 Geometrical cloud depth

We compare geometrical cloud depth as simulated by ICON to that observed during PASCAL. We choose PASCAL cloud radar
 240 and ceilometer observations instead of ACLOUD observations as they provide a continuous dataset in time, which facilitates the comparison of geometrical cloud depth. To better compare the simulations to ground based observations, we use ICON's meteorogram output. It provides profiles of model variables at a certain location at every model timestep compared to the 30 minute output frequency when outputting the whole model domain. For each day simulated, we choose to output the profiles at Polarstern's 12 UTC location. While its position was rather constant from 3 June onward (Wendisch et al., 2019, their Figure

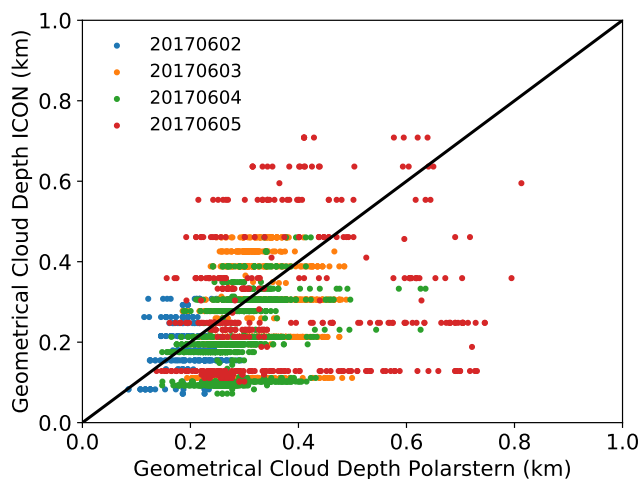


Figure 5. Geometrical cloud depth as simulated by ICON and observed from R/V Polarstern during the period from 2 June to 5 June.

245 2), the ship was still in transit to the ice floe on 2 June. This might introduce some inconsistencies in the comparison to the spatially fixed ICON profiles. As the ship was already relatively far into the marginal sea ice zone, the cloud field should be homogeneous and representative for sea ice covered conditions.

For the model output, a layer within a profile is considered cloud covered if the the total cloud condensate (liquid and ice) is larger than a threshold of 0.05 g m^{-3} . We only assess clouds close to the surface, namely from the ground to 2 km altitude.
250 In this altitude range, we define cloud base/top as the lowest/highest model level a cloud is being simulated within a profile. To derive the observed geometrical cloud depth, we use cloud base height as observed by the laser ceilometer on board R/V Polarstern while cloud top height was derived using the 35 GHz cloud radar (Griesche et al., 2019). Both modeled and observed cloud depths have been temporally interpolated to be on identical timesteps. We acknowledge that such a comparison of geometrical cloud thickness is not a definition aware comparison as it depends on instrument sensitivities and on the chosen
255 threshold of total cloud condensate for diagnosing clouds in the model. Additionally, the rather simple approach is not able to correctly diagnose cloud depth for multi-layer clouds but as stated above, mostly single layer clouds were observed and simulated during the period of interest.

The comparison of geometrical cloud depth for the period from 2 June to 5 June is shown in Figure 5. In general, the geometrical cloud depth in ICON is in fair agreement with the observed geometrical cloud depth even though it shows a slight
260 underestimation compared to the observations. This can be a factor that to some extend contributes to the underestimated cloud optical thickness.

4.2 Cloud microphysical properties

To investigate how cloud microphysical properties contribute to the underestimated cloud optical thickness in ICON, we make use of the suite of in situ instruments that were part of the instrumentation of Polar 6 (Ehrlich et al., 2019). From 2 June to

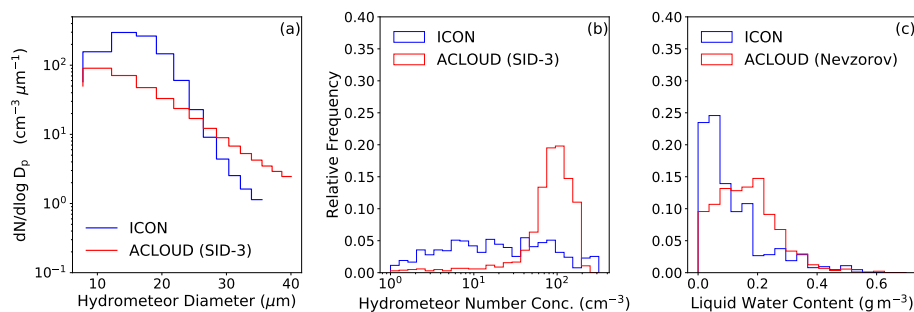


Figure 6. Time-space average particle number size distribution (a) and relative frequency of total particle number in the diameter range from 5 to 40 μm (b), as well as liquid water content (c). All data is averaged over the flights from 2 June to 5 June over sea ice covered region. Filtering for sea ice covered ACLOUD flight sections is done using simulated albedo from ICON.

265 5 June, research flights with Polar 6 were performed on three out of four days (no flight on 3 June). We focus on particle size distribution of hydrometeors and the respective moments, which have been observed by the Small Ice Detector Mark 3 (SID-3) covering a size range of cloud droplets/ice crystals, from 5 to 40 μm . As particle size distributions derived from SID-3 agree well with those from other sensors (such as the Cloud Droplet Probe, CDP) for days when both probes were available (Ehrlich et al., 2019), we are confident that particle size distributions from the SID-3 are best suited for our comparison. In the following, we compare simulated and observed particle size distributions as well as the total (droplets plus ice crystals) particle number concentration (N_d) and the liquid water content (q_c). To be comparable to the particle size distribution from the SID-3, we integrate the size distribution of the two-moment microphysical scheme implemented in ICON within the size bins of the SID-3 for cloud droplets and ice crystals, and add them. Due to relatively warm temperatures in the region of the research flights in early June 2017, only little ice was present in clouds during that period. While we derive the particle number concentration directly from particle size distribution by integrating over the size bins of the SID-3, we use measurements from the Nevzorov probe on Polar 6 to get information on q_c .

270 Figure 6 shows particle number size distributions and the particle number concentration and liquid water content (LWC) for the period from 2 June to 5 June. Looking at the particle size distributions, we find that ICON underestimates the number concentration for hydrometeors smaller than 25 μm , while it overestimates the amount of cloud particles larger than that threshold in comparison to the measurements. As the number of hydrometeors is mainly influenced by the number of small particles, the total amount of hydrometeors is also underestimated in the model. Averaged over all bins, the LWC is underestimated by ICON relative to the LWC derived by the Nevzorov probe as the models overestimates the frequency of occurrence for relatively small LWC values.

5 Discussion

285 According to Equation 3, the underestimated hydrometeor number concentration and LWC both can lead to lower cloud optical thickness in ICON. As not all microphysical schemes in ICON do provide number concentration of cloud droplets and ice



crystals, the calculation of cloud optical properties is simplified in the radiation scheme. As an input for the radiation routines in ICON, a constant profile of cloud droplet number concentration (CDNC) is used, that decreases exponentially with altitude, and LWC for the calculation optical properties of liquid clouds. For open water/sea ice, the assumed surface CDNC within the radiation scheme is 80 cm^{-3} , which is close to the observed cloud hydrometeor number concentrations (Figure 6). Nevertheless, this value is slightly lower than observed the mean of 85 cm^{-3} for the three flight days from 2 June to 5 June. Assuming that the model is able to correctly simulate the LWC, this underestimation would imply lower cloud optical thickness, which would further contribute to the overestimated amount of solar irradiance that reaches the surface. Calculation of optical properties of ice clouds is even further simplified as they are solely depend on the ice water content.

290 Additionally, the LWC in the model is underestimated compared to the observations, which also contributes to the bias in cloud optical thickness in ICON. We attribute the lower LWC to an underestimated number concentration of relatively small cloud droplets (diameters $< 25 \mu\text{m}$), which are commonly observed for this region and season (Mioche et al., 2017). The model also overestimates the number of hydrometeors with diameters larger than $25 \mu\text{m}$. Thus, too few cloud droplets are generated and, therefore, condensational growth and coalescence of the available cloud droplets shifts the size distribution towards larger droplets. Looking at the phase state of precipitation reaching the surface (not shown), we find that the amount of rain is an order of magnitude large than the amount of snow. As temperatures in the atmospheric boundary layer over sea ice were mostly below freezing during the three days analyzed, this precipitation must stems from "warm" rain processes, indicating an relatively active autoconversion process in our set-up. Therefore, autoconversion further contributes to the underestimated LWC by ICON as it acts for a sink of cloud liquid water. Interestingly, the here reported systematic underestimation of hydrometeors is different from the findings by Schemann and Ebell (2020). They conducted simulations for the Ny-Ålesund research station using the ICON model in the large-eddy set-up (ICON-LEM), and compare ground-based cloud radar observations with their ICON-LEM simulations applying a radar forward operator. Besides a different scheme for turbulent transport and activated parameterization of shallow convection in our set-up, as well as corresponding initial/boundary conditions from DWD's operational ICON forecast (instead of ECMWF forecast), the basic set-up is similar to our simulations. Comparing radar reflectivities using contoured frequency by altitude diagrams in mid June 2017 (see Figure 6 in Schemann and Ebell, 2020), they found that for their 75 m domain, the model strongly overestimates the frequency of occurrence for low radar reflectivities/small hydrometeors. They argue that this finding can be related to the way CCN get activated into cloud droplets in the default Seifert-Beheng two-moment microphysical scheme. This was confirmed by ICON-LEM simulations in an Arctic domain by Mech et al. (2020) who implemented different CCN activation scheme (Phillips et al., 2008) within the Seifert-Beheng two-moment microphysics.

300
305
310
315

5.1 Revised activation of CCN in ICON

In the following, we will focus on the issue of the non-matching particle number size distribution compared to ALOUD observations and how it affects total droplet number and LWC of clouds in our simulations. As it has been pointed out by Schemann and Ebell (2020), this process might presently be misrepresented in the model. In its present implementation into ICON, the activation of CCN is parameterized as a function of grid-scale vertical velocity \bar{w} and pressure p as described in

320



Hande et al. (2016):

$$\text{CCN}_{\text{act}} = A(p) \cdot \arctan [B(p) \cdot \log(\bar{w}) + C(p)] + D(p), \quad (4)$$

where the parameters $A(p)$ to $D(p)$ contain information on the vertical profile of CCN and on the activation of CCN with respect to grid-scale vertical velocity \bar{w} . The profile presently used in the two-moment microphysical scheme is a temporally and spatially constant profile taken over Germany for a day in April 2013 as in Heinze et al. (2017). This CCN activation profile is not representative for the amount of CCN in the Arctic domain, as the CCN concentration in the Arctic is much lower. As stated in Schemann and Ebell (2020), the overestimated frequency of occurrence for low radar reflectivities/small hydrometeors can be related to this unsuitable CCN profile.

It is plausible that the relatively low hydrometeor number concentration is related to the coarser resolution in our ICON simulations. A realistic simulation of turbulence and cloud-scale vertical motion is crucial for Arctic mixed-phase clouds (Raubert and Tokay, 1991; Korolev and Field, 2008; Shupe et al., 2008). As the number of activated CCN is a function of grid-scale vertical velocity, it is likely that our simulations at 1.2 km resolution do not sufficiently resolve in-cloud vertical motion and turbulence (Tonttila et al., 2011). This is consistent with the fact that characteristic eddy size in Arctic mixed-phase clouds is less than 1 km (Pinto, 1998). Fan et al. (2011) suggested that only horizontal model resolutions of less than 100 m are able to resolve major dynamic features that contribute to vertical motion in Arctic mixed-phase clouds. Not being able to resolve those features consequently affects particle size distributions and its moments like number concentration as too few droplets are activated (Morrison and Pinto, 2005).

To account for subgrid-scale vertical motion, vertical velocity in the aerosol activation in larger scale models is often parameterized as a function of specific turbulent kinetic energy (Ghan et al., 1997; Lohmann et al., 1999), TKE, which is defined as:

$$\text{TKE} = \frac{1}{2} \cdot \overline{(u'^2 + v'^2 + w'^2)}, \quad (5)$$

where the u', v', w' are the subgrid-scale deviations from grid-scale velocity and the overbar denotes grid-box average. To explore the effects of including sub-grid scale vertical velocity in the Hande et al. (2016) CCN activation parametrization, we choose to follow a similar approach as proposed in Ghan et al. (1997), who assume the sub-grid vertical velocity in a grid box to follow a Gaussian distribution $P(w | \bar{w}, \sigma_w^2)$. The grid box averaged number of activated CCN can, therefore, be written as the integral over positive vertical velocities:

$$\overline{\text{CCN}_{\text{act}}} = \int_0^{\infty} P(w | \bar{w}, \sigma_w^2) \cdot \text{CCN}_{\text{act}}(w) dw. \quad (6)$$

To numerically solve the integral in Equation 6, a relatively simple trapezoidal integration is employed using 50 equally spaced bins in a $\pm 3\sigma_w$ range around \bar{w} .

If it is assumed that sub-grid scale motion in low-level Arctic mixed-phase clouds is isotropic ($u'^2 = v'^2 = w'^2$), as proposed by Pinto (1998), the variance of vertical velocity can be expressed as function of TKE as follows (Morrison and Pinto, 2005):

$$\sigma_w^2 = w'^2 = \frac{2}{3} \cdot \text{TKE}. \quad (7)$$

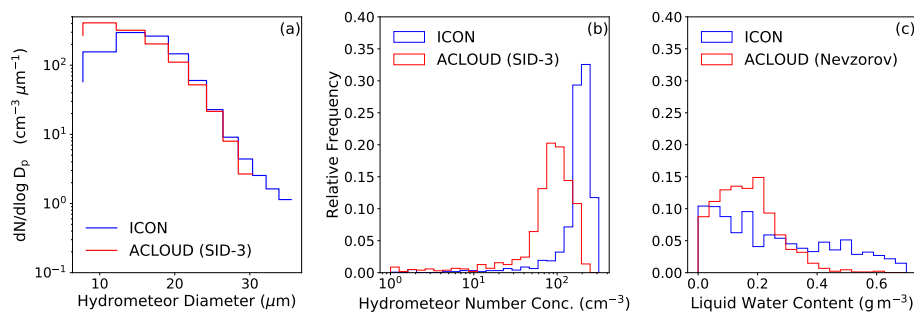


Figure 7. As Figure 6 but for the revised CCN activation. All red lines (ACLOUD) are identical to the corresponding red lines in Figure 6.

Using turbulence measurements on a tethered balloon during the PASCAL ice floe operations, Egerer et al. (2019) showed that isotropic turbulence is a valid assumption for a subset of days during PASCAL that have been analyzed in their study. We, nevertheless, are aware that isotropic sub-grid scale motion in Arctic clouds cannot be assumed for all conditions (Curry et al., 1988; Finger and Wendling, 1990).

The effects of this revised CCN activation for the period from 2 June to 5 June are shown in Figure 7. Compared to the original activation parameterization, the model shows a much closer agreement with the measurements, although an overestimation of hydrometeors with diameters less than $20 \mu\text{m}$ is simulated, while it underestimates the number of hydrometeors larger than $30 \mu\text{m}$. As the number of small hydrometeors governs the total number of hydrometeors, their overestimation now also leads to an overestimated number of total hydrometeors in the whole diameter range between 5 and $40 \mu\text{m}$. The particle size distribution now is in better agreement with the findings by Schemann and Ebell (2020), as we find an overestimation of smaller hydrometeors and underestimated number concentration of larger hydrometeors compared to in situ observations. The shift of the particle size distribution towards smaller hydrometeors can be related to the unsuited CCN profile within the activation parameterization. The increased number of hydrometeors also affects the LWC, which is more evenly distributed over the mass density bins, ranging up to 0.6 g m^{-3} . Compared to the ACloud observations, small values of liquid water content less than 0.3 g m^{-3} are underestimated, while values larger than that threshold are simulated more frequently in the revised CCN activation.

The presently used CCN activation profile was originally derived for spring conditions in Germany, where one would expect a much higher load of CCN compared to the Arctic. To have a more realistic representation of CCN, a dedicated simulation with a model that is able to represent the formation and transport of aerosols would be necessary. We opt against this approach and just scale the number of activated CCN from the default profile using a scaling factor of 0.4. A more elaborate description why this scaling factor was used is given in Appendix A. The chosen scaling factor now results in an underestimated number of hydrometeors smaller than $22 \mu\text{m}$ as it is shown in Figure 8, while hydrometeors with larger diameters are overestimated by the model. Looking at the hydrometeors number concentration, the chosen scaling factor shifts the simulated distribution towards smaller hydrometeor concentrations that consequently results in a slight underestimation of hydrometeors compared to the observations. This indicates that the chosen scaling factor is slightly too effective in reducing the number of activated CCN.

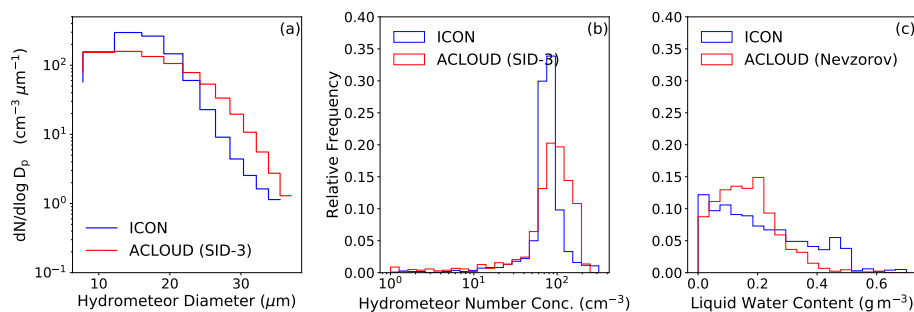


Figure 8. As Figure 7 but with scaled number of activated CCN by a factor of 0.4. All red lines (ACLOUD) are identical to the corresponding red lines in Figure 6.

Compared to Figure 7, high values of liquid water content larger than 0.3 g m^{-3} occur less frequently when scaling the number of activated CCN, but there is still a slight underestimation in the frequency of occurrence for LWC values between 0.1 g m^{-3} and 0.3 g m^{-3} . Even though scaled, the overall shape of the profile of activated CCN as a function of vertical velocity remains unchanged. A different aerosol composition or just a different vertical profile of aerosols alter the shape of the profile, which might also lead to biases in the number of activated CCN. This emphasizes the need for an CCN activation profile that is better suited for an Arctic environment, which has also been proposed by Schemann and Ebell (2020).

The effect of the different CCN activation set-ups on the CRE for all flights from 2 June to 5 June is shown in Figure 9 (a)-(c). We would like to point out that the cloud fields between the respective CCN activation set-ups vary. For that reason, the number of available datapoints for which the threshold for sea ice coverage and cloudy conditions are fulfilled at the same time, differ between the runs due to the filtering that is employed. Similar to the histograms in Figure 4, which cover all flights used in this comparison, the warming effect of clouds at the surface is overestimated when looking at the period from 2 June to 5 June. For the revised CCN activation, the increase in LWC reflects on the surface CRE, which now has a small negative bias compared to the ACloud observations. Because of the aforementioned constant profile of cloud droplet number concentrations in the calculation of the effective radius within the radiation scheme, this negative bias would be more strongly expressed if the actual cloud droplet number concentration from the microphysical scheme would be used (see subsection 5.2). When scaling the activated number of CCN by a factor of 0.4, the CRE is still overestimated by ICON compared to observations even though the positive bias in the median could be reduced by approximately 5 W m^{-1} . As downscaling the number of activated CCN by a factor of 0.4 was already slightly too effective in reducing the hydrometeor number, a larger scaling factor might be able to further decrease the CRE in the model.

5.2 Coupling of hydrometeor number concentration to radiation

As already discussed above, there is an inconsistency between the hydrometeor number concentration derived in the two-moment microphysics and used in the radiation routines. In the following, we therefore explore the effect of making the hydrometeor concentrations consistent between the two parametrizations. As input for the calculation of optical properties,



ICON uses cloud droplet/ice crystal effective radius, which is defined as the ratio of the third to the second moment of the size distribution. Previously, effective radii were computed as a function solely of specific masses.

To ensure consistency with the size distributions in the Seifert-Beheng two-moment scheme, we calculate the effective radii from the used gamma distribution (see Appendix B for the derivation). This new implementation has already been used in
405 Costa-Surós et al. (2019). In Figure 9 (d)-(f), the biggest difference to the uncoupled hydrometeor number concentrations (Figure 9 (a)-(c)) can be seen in the histograms for the revised CCN activation (Figure 9 (e)). In this set-up, the CRE is underestimated compared to observations due to higher hydrometeor concentration, which is now also considered in the radiation parameterization. For the revised and scaled CCN activation, only little differences are simulated between coupled and uncoupled hydrometeor concentration. As stated above, the fixed cloud droplet number concentration in the default radiation routines
410 is already relatively close to the hydrometeor concentration observed for the flights from 2 June to 5 June. Nevertheless, compared to the observations, the median value of the CRE in ICON in Figure 9 (e) is closest to the observed values, even though they are still slightly overestimated. Altogether, the revised CCN activation with a scaled CCN activation and coupled hydrometeor now results in a positive bias of only approximately 6 W m^{-2} . The effect on surface CRE of the coupling of hydrometeor number concentration to radiation for this period is relatively low (1 W m^{-2} , see Figure 9 (c) and (e)), as the assumed number
415 concentration in the default set up and the number concentrations from two-moment microphysical scheme in the revised and scaled CCN activation are in a similar range. As can be seen from Figure 9 (b) and (e), if the CDNC profile in the microphysics deviates from the profile in the radiation, there can be quiet substantial differences due to a more realistic representation of the Twomey effect (Twomey, 1977), which can be important for relatively clean/polluted situations.

6 Conclusions

420 In this study, we use observational data from the ALOUD and PASCAL campaigns (Wendisch et al., 2019) to compare it to limited-area simulations with the ICON atmospheric model at kilometer-scale resolution. While the model compares well to the observations in its ability to simulate the four cloud-surface radiation regimes in the Arctic, it severely underestimates cloud radiative effects in the solar spectrum. This is despite a slight overestimation of the geometrical cloud thickness and attributable to too small droplet number concentrations and too little liquid water content. We showed that it is crucial to correctly simulate
425 in-cloud turbulence in Arctic clouds, which is essential to correctly simulate hydrometeor number concentration and liquid water content.

As reported by Stevens et al. (2020), the representation of clouds in atmospheric models benefits from higher resolved simulation. Nevertheless, long time, global simulations at hectometer scale will not be feasible in the foreseeable future (Schneider et al., 2017), whereas climate projections at kilometer-scale can be achievable (Stevens et al., 2019). It is therefore important
430 to especially improve models on such scales to enable them to make realistic simulation. As shown in this study, aircraft observations are a valuable source of information and can be used for evaluating and improving the representation of physical processes for models at kilometer-scale. The results presented in our study might also be beneficial to the representation of clouds in ICON in other regions, where clouds are also turbulence-driven.

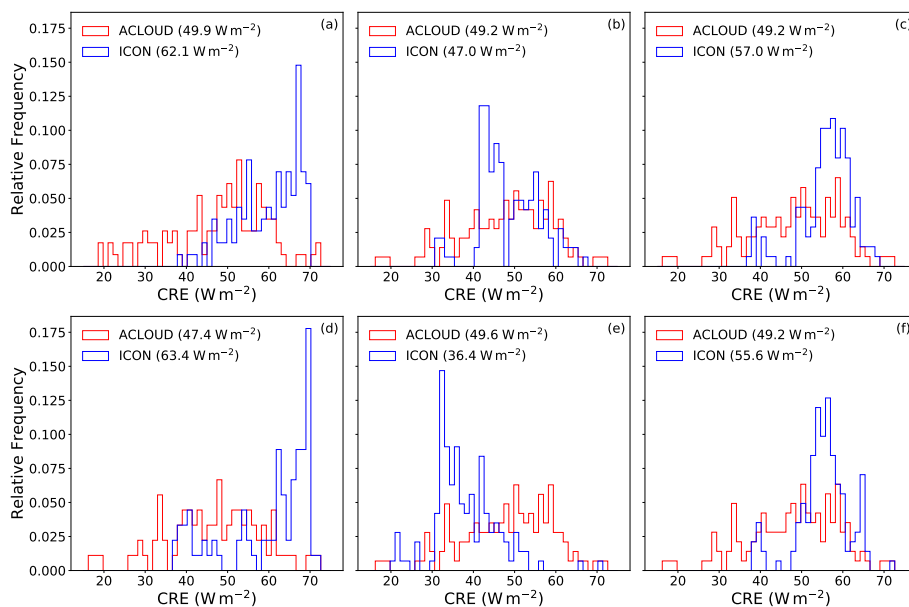


Figure 9. As Fig. 4a, but for the flights from 2 June to 5 June only, for the default set-up (a), for the revised CCN activation (b) and for the revised CCN activation with scaled number of activated CCN by a factor of 0.4 (c). The bottom row (d-f) as the top row but with hydrometeor number concentration coupled to radiation.

Data availability. The ICON model output data used in this study is stored at the German Climate Computing Center (DKRZ) and is available upon request from the corresponding author. The observational data from the ACloud/PASCAL campaigns archived on PANGAEA repository and can be accessed from the following DOIs: broadband (solar and terrestrial) irradiances (<https://doi.org/10.1594/PANGAEA.902603>, Stapf et al., 2019b), Small Ice Detector Mark 3 (SID-3) (<https://doi.org/10.1594/PANGAEA.900261>, Schnaiter and Järvinen, 2019), Nevzorov probe (<https://doi.org/10.1594/PANGAEA.906658>, Chechin, 2019) and cloud radar 35 GHz cloud radar onboard of R/V Polarstern (<https://doi.org/10.1594/PANGAEA.899895>, Griesche et al., 2019).

440 Appendix A: Scaling of the default CCN profile

In this study, we decided to scale to default CCN profile in ICON to match values representative for the Arctic. The scaling factor is derived from aerosol mass mixing ratios from the re-analysis of atmospheric composition of the Copernicus Atmospheric Monitoring Service (CAMS; Inness et al., 2019), which assimilated MODerate Resolution Imaging Spectroradiometer (MODIS) aerosol retrievals (Levy et al., 2013) into the ECMWF model (Benedetti et al., 2009). We computed the number of activated CCN for various vertical velocities and also supersaturation for a sea ice covered domain north of Svalbard during the period from 2 June to 5 June following the approach of Block (2018). Close to the surface, the number of activated CCN at a supersaturation of 0.5 % in this dataset is approximately 45 cm^{-3} . This value is on the lower end of the observed number concentrations of activated CCN during PASCAL, which were in a range of 40 to 80 cm^{-3} during this period (Wendisch et al.,



Table A1. Scaling factor that minimizes the mean squared error of the scaled default activation profile in ICON and the activation profile derived from CAMS for several vertical velocities in an altitude band from the surface to 700 hPa.

w (m s ⁻¹)	0.01	0.03	0.08	0.22	0.60
Scaling factor	0.5	0.4	0.4	0.4	0.3

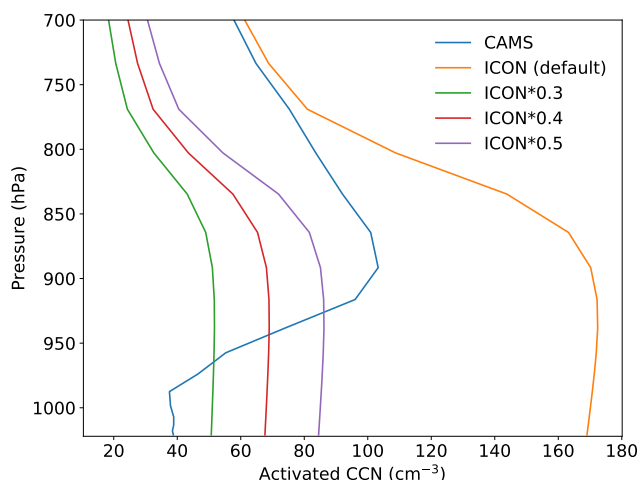


Figure A1. Profile of activated CCN at 0.08 m s^{-1} from CAMS and from the default profile in ICON. Additionally, a subset of scaled ICON profiles is shown.

2019, their Figure 10).

450 To decide which scaling factor to use, we looked for a scaling factor (in steps of 0.05) that minimizes the mean squared error
of the scaled profile and the profile derived from CAMS for several vertical velocities in an altitude band from the surface
to 700 hPa. From Table A1, we find that a scaling factor of 0.4 is a good compromise for relatively low vertical velocities in
Arctic clouds. Even though scaled to best match the CAMS profile, the overall shape of the profile of activated CCN in ICON
remains unchanged. Figure A1 shows that the default profile strongly overestimates the number of activated CCN close to
455 the surface while nicely matches the CAMS profile for altitudes higher than 800 hPa. As almost all clouds from 2 June to 5
June were below that altitude, it is more important to correctly represent the number of activated aerosol close to the surface.
The number of activated CCN is almost constant up to 850 hPa, whereas the number of activated CCN in the CAMS profile
increases with altitude. Even though we cannot match the shape of the activation profile, a scaling factor of 0.4 should represent
an approximate average up to 850 hPa.



460 Appendix B: Derivation of effective radius from gamma distribution

To describe the particle size distributions of all hydrometeor categories in the Seifert-Beheng two-moment microphysical scheme (Seifert and Beheng, 2006), a modified gamma distribution is used:

$$f(x) = Ax^\nu \exp(-\lambda x^\mu), \quad (\text{B1})$$

where x is the particle mass and ν and μ are the parameters of the distribution for the respective hydrometeor category. A and
 465 λ can be expressed by the number/mass densities and the parameters ν and μ (Eq. 80, Seifert and Beheng, 2006). Following Petty and Huang (2011), the k -th moment M_k of such a modified gamma distribution can be expressed as follows:

$$M_k = \frac{A}{\mu} \frac{\Gamma\left(\frac{\nu+k+1}{\mu}\right)}{A^{(\nu+k+1)/\mu}}. \quad (\text{B2})$$

The ratiion between 3th and 2th moment can, therefore, be written as:

$$\frac{M_3}{M_2} = \frac{\Gamma\left(\frac{\nu+4}{\mu}\right)}{\Gamma\left(\frac{\nu+3}{\mu}\right)} \lambda^{\frac{-1}{\mu}}. \quad (\text{B3})$$

470 To obtain the effective radius, Equation B1 has to be first converted into a function of radius. According to Eq. 54 in Petty and Huang (2011) the particle size distribution as a function of radius $f(r)$ can be written as:

$$A_r r^{\nu_r} \exp(-\lambda_r r^{\mu_r}) = Ax(r)^\nu \exp[-\lambda r^\mu] \frac{dx}{dr}, \quad (\text{B4})$$

The particle mass as a function of radius $x(r)$ in the Seifert-Beheng two-moment microphysical scheme is defined as follows:

$$x(r) = \left(\frac{2r}{a}\right)^{\frac{1}{b}}, \quad (\text{B5})$$

475 which differs from the functional relationship given in Table 1 in Petty and Huang (2011), as the values for a and b are defined differently (see Table 1 in Seifert and Beheng, 2006). Therefore:

$$\frac{dx}{dr} = \left(\frac{2}{a}\right)^{\frac{1}{b}} \frac{1}{b} r^{\left(\frac{1}{b}-1\right)}. \quad (\text{B6})$$

Inserting Equation B5 and Equation B6 into Equation B4 and comparing the respective parameters for radius and mass in Equation B1, we find the following conversion relationships for the parameters in the particle size distribution:

$$480 A_r = \frac{A}{b} \left(\frac{2}{a}\right)^{\frac{\nu+1}{b}}, \quad \nu_r = \frac{\nu+1-b}{b}, \quad \lambda_r = \lambda \left(\frac{2}{a}\right)^{\frac{\mu}{b}}, \quad \mu_r = \frac{\mu}{b}. \quad (\text{B7})$$

By inserting those parameters into Equation B3 and applying the functional dependencies for A and λ from Eq. 80 in Seifert and Beheng (2006), the effective radius r_{eff} can be written as follows:

$$r_{\text{eff}} = \left[\frac{\Gamma\left(\frac{\nu+1}{\mu}\right)}{\Gamma\left(\frac{\nu+2}{\mu}\right)} \right]^b \left(\frac{q}{N}\right)^b \frac{a}{2} \frac{\Gamma\left(\frac{\nu+1+3b}{\mu}\right)}{\Gamma\left(\frac{\nu+1+2b}{\mu}\right)}, \quad (\text{B8})$$

where q and N are the mass and number density for the respective hydrometeor category.



485 *Author contributions.* JK, JS, MW and JQ this conceived this study. DK helped setting up the input data for the ICON runs and gave valuable expertise on how to run the model in a limited area set-up. JK and JS prepared and analyzed the model and observational data, respectively. All of the authors assisted with the interpretation of the results. JK prepared the manuscript with contributions from all co-authors.

Competing interests. The authors declare that they have no conflict of interest.

Disclaimer. TEXT

490 *Acknowledgements.* We gratefully acknowledge the funding by the Deutsche Forschungsgemeinschaft (DFG, German Research Foundation) - 268020496 - TRR 172, within the Transregional Collaborative Research Center “ArctiC Amplification: Climate Relevant Atmospheric and SurfaCe Processes, and Feedback Mechanisms (AC)³. The ICON model is jointly developed by German Weather Service (DWD) and the Max Planck Institute for Meteorology, Hamburg, and we thank the colleagues for making the model available to the research community. We furthermore thank the colleagues that participated in the ALOUD/PASCAL campaigns for providing the datasets used in this study.

495 Simulations were conducted at the German Climate Computing Center (Deutsches Klimarechenzentrum, DKRZ). We thank Axel Seifert, Kerstin Ebell and Vera Schemann for giving valuable comments on this manuscript.



References

- Baldauf, M., Seifert, A., Förstner, J., Majewski, D., Raschendorfer, M., and Reinhardt, T.: Operational Convective-Scale Numerical Weather Prediction with the COSMO Model: Description and Sensitivities, *Monthly Weather Review*, 139, 3887–3905, <https://doi.org/10.1175/MWR-D-10-05013.1>, 2011.
- Barton, N. P., Klein, S. A., Boyle, J. S., and Zhang, Y. Y.: Arctic synoptic regimes: Comparing domain-wide Arctic cloud observations with CAM4 and CAM5 during similar dynamics, *Journal of Geophysical Research Atmospheres*, 117, <https://doi.org/10.1029/2012JD017589>, 2012.
- Bechtold, P., Köhler, M., Jung, T., Doblas-Reyes, F., Leutbecher, M., Rodwell, M. J., Vitart, F., and Balsamo, G.: Advances in simulating atmospheric variability with the ECMWF model: From synoptic to decadal time-scales, *Quarterly Journal of the Royal Meteorological Society*, 134, 1337–1351, <https://doi.org/10.1002/qj.289>, <http://doi.wiley.com/10.1002/qj.289>, 2008.
- Benedetti, A., Morcrette, J.-J., Boucher, O., Dethof, A., Engelen, R. J., Fisher, M., Flentje, H., Huneeus, N., Jones, L., Kaiser, J. W., Kinne, S., Mangold, A., Razinger, M., Simmons, A. J., and Suttie, M.: Aerosol analysis and forecast in the European Centre for Medium-Range Weather Forecasts Integrated Forecast System: 2. Data assimilation, *Journal of Geophysical Research*, 114, D13 205, <https://doi.org/10.1029/2008JD011115>, 2009.
- Bentley, J. L.: Multidimensional binary search trees used for associative searching, *Communication Association for Computing Machinery*, 18, 509–517, <https://doi.org/10.1145/361002.361007>, 1975.
- Block, K.: Aerosol-Cloud-Radiation interactions in regimes of liquid water clouds, Phd thesis, University Leipzig, https://research.uni-leipzig.de/climate/block_{_}karoline_{_}{_}phd_{_}{_}2018.pdf, 2018.
- Block, K., Schneider, F. A., Mülmenstädt, J., Salzmann, M., and Quaas, J.: Climate models disagree on the sign of total radiative feedback in the Arctic, *Tellus A: Dynamic Meteorology and Oceanography*, 72, 1–14, <https://doi.org/10.1080/16000870.2019.1696139>, 2020.
- Bodas-Salcedo, A., Webb, M. J., Bony, S., Chepfer, H., Dufresne, J. L., Klein, S. A., Zhang, Y., Marchand, R., Haynes, J. M., Pincus, R., and John, V. O.: Bodas-Salcedo, A., Webb, M. J., Bony, S., Chepfer, H., Dufresne, J. L., Klein, S. A., Zhang, Y., Marchand, R., Haynes, J. M., Pincus, R. and John, V. O.: COSP: Satellite simulation software for model assessment, *Bull. Am. Meteorol. Soc.*, 92(8), 1023–1043, *Bulletin of the American Meteorological Society*, 92, 1023–1043, <https://doi.org/10.1175/2011BAMS2856.1>, 2011.
- Boeke, R. C. and Taylor, P. C.: Evaluation of the Arctic surface radiation budget in CMIP5 models, *Journal of Geophysical Research: Atmospheres*, 121, 8525–8548, <https://doi.org/10.1002/2016JD025099>, 2016.
- Cesana, G., Kay, J. E., Chepfer, H., English, J. M., and De Boer, G.: Ubiquitous low-level liquid-containing Arctic clouds: New observations and climate model constraints from CALIPSO-GOCCP, *Geophysical Research Letters*, 39, <https://doi.org/10.1029/2012GL053385>, 2012.
- Chechin, D.: Liquid water content measured by the Nevzorov probe during the aircraft ALOUD campaign in the Arctic, <https://doi.org/10.1594/PANGAEA.906658>, 2019.
- Costa-Surós, M., Sourdeval, O., Acquistapace, C., Baars, H., Carbajal Henken, C., Genz, C., Hesemann, J., Jimenez, C., König, M., Kretzschmar, J., Madenach, N., Meyer, C., Schrödner, R., Seifert, P., Senf, F., Brueck, M., Cioni, G., Engels, J. F., Fieg, K., Gorges, K., Heinze, R., Siligam, P. K., Burkhardt, U., Crewell, S., Hoose, C., Seifert, A., Tegen, I., and Quaas, J.: Detection and attribution of aerosol-cloud interactions in large-domain large-eddy simulations with ICON, *Atmospheric Chemistry and Physics Discussions*, <https://doi.org/10.5194/acp-2019-850>, 2019.
- Curry, J. A., Ebert, E. E., and Herman, G. F.: Mean and turbulence structure of the summertime Arctic cloudy boundary layer, *Quarterly Journal of the Royal Meteorological Society*, 114, 715–746, <https://doi.org/10.1002/qj.49711448109>, 1988.



- Dipankar, A., Stevens, B., Heinze, R., Moseley, C., Zängl, G., Giorgetta, M., and Brdar, S.: Large eddy simulation using the general circulation model ICON, *Journal of Advances in Modeling Earth Systems*, 7, 963–986, <https://doi.org/10.1002/2015MS000431>, 2015.
- 535 Egerer, U., Gottschalk, M., Siebert, H., Ehrlich, A., and Wendisch, M.: The new BELUGA setup for collocated turbulence and radiation measurements using a tethered balloon: First applications in the cloudy Arctic boundary layer, *Atmospheric Measurement Techniques*, 12, 4019–4038, <https://doi.org/10.5194/amt-12-4019-2019>, 2019.
- Ehrlich, A., Wendisch, M., Lüpkes, C., Buschmann, M., Bozem, H., Chechin, D., Clemen, H.-C., Dupuy, R., Eppers, O., Hartmann, J., Herber, A., Jäkel, E., Järvinen, E., Jourdan, O., Kästner, U., Kliesch, L.-L., Köllner, F., Mech, M., Mertes, S., Neuber, R., Ruiz-Donoso, E., Schnaiter, M., Schneider, J., Stapf, J., and Zanatta, M.: A comprehensive in situ and remote sensing data set from the Arctic CLOUD Observations Using airborne measurements during polar Day (ACLOUD) campaign, *Earth System Science Data*, 11, 1853–1881, <https://doi.org/10.5194/essd-11-1853-2019>, 2019.
- 540 English, J. M., Gettelman, A., and Henderson, G. R.: Arctic Radiative Fluxes: Present-Day Biases and Future Projections in CMIP5 Models, *Journal of Climate*, 28, 6019–6038, <https://doi.org/10.1175/JCLI-D-14-00801.1>, 2015.
- Fan, J., Ghan, S., Ovchinnikov, M., Liu, X., Rasch, P. J., and Korolev, A.: Representation of Arctic mixed-phase clouds and the Wegener-Bergeron-Findeisen process in climate models: Perspectives from a cloud-resolving study, *Journal of Geophysical Research*, 116, D00T07, <https://doi.org/10.1029/2010JD015375>, 2011.
- Finger, J. E. and Wendling, P.: Turbulence Structure of Arctic Stratus Clouds Derived from Measurements and Calculations, *Journal of the Atmospheric Sciences*, 47, 1351–1373, [https://doi.org/10.1175/1520-0469\(1990\)047<1351:TSOASC>2.0.CO;2](https://doi.org/10.1175/1520-0469(1990)047<1351:TSOASC>2.0.CO;2), 1990.
- 550 Flores, H. and Macke, A.: The Expeditions PS106/1 and 2 of the Research Vessel POLARSTERN to the Arctic Ocean in 2017, *Berichte zur Polar- und Meeresforschung*, 714, https://doi.org/10.2312/BzPM_0714_2017, https://doi.org/10.2312/BzPM_{_}0714_{_}2017, 2018.
- Ghan, S. J., Leung, L. R., Easter, R. C., and Abdul-Razzak, H.: Prediction of cloud droplet number in a general circulation model, *Journal of Geophysical Research: Atmospheres*, 102, 21 777–21 794, <https://doi.org/10.1029/97JD01810>, 1997.
- 555 Giorgetta, M. A., Brokopf, R., Crueger, T., Esch, M., Fiedler, S., Helmert, J., Hohenegger, C., Kornblüeh, L., Köhler, M., Manzini, E., Mauritsen, T., Nam, C., Raddatz, T., Rast, S., Reinert, D., Sakradzija, M., Schmidt, H., Schneck, R., Schnur, R., Silvers, L., Wan, H., Zängl, G., and Stevens, B.: ICON-A, the Atmosphere Component of the ICON Earth System Model: I. Model Description, *Journal of Advances in Modeling Earth Systems*, 10, 1613–1637, <https://doi.org/10.1029/2017MS001242>, 2018.
- Griesche, H., Seifert, P., Engelmann, R., Radenz, M., and Bühl, J.: OCEANET Cloud radar Mira-35 during POLARSTERN cruise PS106, <https://doi.org/10.1594/PANGAEA.899895>, <https://doi.org/10.1594/PANGAEA.899895>, 2019.
- 560 Grosvenor, D. P., Sourdeval, O., Zuidema, P., Ackerman, A., Alexandrov, M. D., Bennartz, R., Boers, R., Cairns, B., Chiu, J. C., Christensen, M., Deneke, H., Diamond, M., Feingold, G., Fridlind, A., Hünerbein, A., Knist, C., Kollias, P., Marshak, A., McCoy, D., Merk, D., Painemal, D., Rausch, J., Rosenfeld, D., Russchenberg, H., Seifert, P., Sinclair, K., Stier, P., van Diedenhoven, B., Wendisch, M., Werner, F., Wood, R., Zhang, Z., and Quaas, J.: Remote Sensing of Droplet Number Concentration in Warm Clouds: A Review of the Current State of Knowledge and Perspectives, *Reviews of Geophysics*, 56, 409–453, <https://doi.org/10.1029/2017RG000593>, 2018.
- Hande, L. B., Engler, C., Hoose, C., and Tegen, I.: Parameterizing cloud condensation nuclei concentrations during HOPE, *Atmospheric Chemistry and Physics*, 16, 12 059–12 079, <https://doi.org/10.5194/acp-16-12059-2016>, 2016.
- Heinze, R., Dipankar, A., Henken, C. C., Moseley, C., Sourdeval, O., Trömel, S., Xie, X., Adamidis, P., Ament, F., Baars, H., Barthlott, C., Behrendt, A., Blahak, U., Bley, S., Brdar, S., Brueck, M., Crewell, S., Deneke, H., Di Girolamo, P., Evaristo, R., Fischer, J., Frank, C., Friederichs, P., Göcke, T., Gorges, K., Hande, L., Hanke, M., Hansen, A., Hege, H. C., Hoose, C., Jahns, T., Kalthoff, N., Klocke, D., Kneifel, S., Knippertz, P., Kuhn, A., van Laar, T., Macke, A., Maurer, V., Mayer, B., Meyer, C. I., Muppa, S. K., Neggers, R. A. J.,
- 570



- Orlandi, E., Pantillon, F., Pospichal, B., Röber, N., Scheck, L., Seifert, A., Seifert, P., Senf, F., Siligam, P., Simmer, C., Steinke, S., Stevens, B., Wapler, K., Weniger, M., Wulfmeyer, V., Zängl, G., Zhang, D., and Quaas, J.: Large-eddy simulations over Germany using ICON: a comprehensive evaluation, *Quarterly Journal of the Royal Meteorological Society*, 143, 69–100, <https://doi.org/10.1002/qj.2947>, 2017.
- 575 Inness, A., Ades, M., Agustí-Panareda, A., Barré, J., Benedictow, A., Blechschmidt, A.-M., Dominguez, J. J., Engelen, R., Eskes, H., Flemming, J., Huijnen, V., Jones, L., Kipling, Z., Massart, S., Parrington, M., Peuch, V.-H., Razinger, M., Remy, S., Schulz, M., and Suttie, M.: The CAMS reanalysis of atmospheric composition, *Atmospheric Chemistry and Physics*, 19, 3515–3556, <https://doi.org/10.5194/acp-19-3515-2019>, 2019.
- Jäkel, E., Stapf, J., Wendisch, M., Nicolaus, M., Dorn, W., and Rinke, A.: Validation of the sea ice surface albedo scheme of the regional
580 climate model HIRHAM–NAOSIM using aircraft measurements during the ALOUD/PASCAL campaigns, *The Cryosphere*, 13, 1695–1708, <https://doi.org/10.5194/tc-13-1695-2019>, 2019.
- Karlsson, J. and Svensson, G.: Consequences of poor representation of Arctic sea-ice albedo and cloud-radiation interactions in the CMIP5 model ensemble, *Geophysical Research Letters*, 40, 4374–4379, <https://doi.org/10.1002/grl.50768>, 2013.
- Kay, J. E., L’Ecuyer, T., Chepfer, H., Loeb, N., Morrison, A., and Cesana, G.: Recent Advances in Arctic Cloud and Climate Research, *Current Climate Change Reports*, pp. 1–11, <https://doi.org/10.1007/s40641-016-0051-9>, 2016.
- 585 Klocke, D., Brueck, M., Hohenegger, C., and Stevens, B.: Rediscovery of the doldrums in storm-resolving simulations over the tropical Atlantic, *Nature Geoscience*, 10, 891–896, <https://doi.org/10.1038/s41561-017-0005-4>, 2017.
- Knudsen, E. M., Heinold, B., Dahlke, S., Bozem, H., Crewell, S., Gorodetskaya, I. V., Heygster, G., Kunkel, D., Maturilli, M., Mech, M., Viceto, C., Rinke, A., Schmithüsen, H., Ehrlich, A., Macke, A., Lüpkes, C., and Wendisch, M.: Meteorological conditions during
590 the ALOUD/PASCAL field campaign near Svalbard in early summer 2017, *Atmospheric Chemistry and Physics*, 18, 17995–18022, <https://doi.org/10.5194/acp-18-17995-2018>, 2018.
- Knust, R.: Polar Research and Supply Vessel POLARSTERN operated by the Alfred-Wegener-Institute, *Journal of large-scale research facilities JLSRF*, 3, A119, <https://doi.org/10.17815/jlsrf-3-163>, <http://jlsrf.org/index.php/lsf/article/view/163>, 2017.
- Korolev, A. and Field, P. R.: The Effect of Dynamics on Mixed-Phase Clouds: Theoretical Considerations, *Journal of the Atmospheric
595 Sciences*, 65, 66–86, <https://doi.org/10.1175/2007JAS2355.1>, 2008.
- Korolev, A. V., Strapp, J. W., Isaac, G. A., and Nevzorov, A. N.: The Nevzorov Airborne Hot-Wire LWC–TWC Probe: Principle of Operation and Performance Characteristics, *Journal of Atmospheric and Oceanic Technology*, 15, 1495–1510, [https://doi.org/10.1175/1520-0426\(1998\)015<1495:TNAHWL>2.0.CO;2](https://doi.org/10.1175/1520-0426(1998)015<1495:TNAHWL>2.0.CO;2), 1998.
- Kretzschmar, J., Salzmann, M., Mülmenstädt, J., and Quaas, J.: Arctic clouds in ECHAM6 and their sensitivity to cloud microphysics and
600 surface fluxes, *Atmospheric Chemistry and Physics*, 19, 10571–10589, <https://doi.org/10.5194/acp-19-10571-2019>, 2019.
- Levy, R. C., Mattoo, S., Munchak, L. A., Remer, L. A., Sayer, A. M., Patadia, F., and Hsu, N. C.: The Collection 6 MODIS aerosol products over land and ocean, *Atmospheric Measurement Techniques*, 6, 2989–3034, <https://doi.org/10.5194/amt-6-2989-2013>, <https://www.atmos-meas-tech.net/6/2989/2013/>, 2013.
- Loewe, K., Ekman, A. M. L., Paukert, M., Sedlar, J., Tjernström, M., and Hoose, C.: Modelling micro- and macrophysical contributors to
605 the dissipation of an Arctic mixed-phase cloud during the Arctic Summer Cloud Ocean Study (ASCOS), *Atmospheric Chemistry and Physics*, 17, 6693–6704, <https://doi.org/10.5194/acp-17-6693-2017>, 2017.
- Lohmann, U., Feichter, J., Chuang, C. C., and Penner, J. E.: Prediction of the number of cloud droplets in the ECHAM GCM, *Journal of Geophysical Research: Atmospheres*, 104, 9169–9198, <https://doi.org/10.1029/1999JD900046>, 1999.



- Lohmann, U., Quaas, J., Kinne, S., and Feichter, J.: Different Approaches for Constraining Global Climate Models of the Anthropogenic Indirect Aerosol Effect, *Bulletin of the American Meteorological Society*, 88, 243–250, <https://doi.org/10.1175/BAMS-88-2-243>, 2007.
- Mech, M., Maahn, M., Kneifel, S., Ori, D., Orlandi, E., Kollias, P., Schemann, V., and Crewell, S.: PAMTRA 1.0: A Passive and Active Microwave radiative TRANSfer tool for simulating radiometer and radar measurements of the cloudy atmosphere, *Geoscientific Model Development Discussions*, <https://doi.org/10.5194/gmd-2019-356>, 2020.
- Mioche, G., Jourdan, O., Delanoë, J., Gourbeyre, C., Febvre, G., Dupuy, R., Monier, M., Szczap, F., Schwarzenboeck, A., and Gayet, J.-F.: Vertical distribution of microphysical properties of Arctic springtime low-level mixed-phase clouds over the Greenland and Norwegian seas, *Atmospheric Chemistry and Physics*, 17, 12 845–12 869, <https://doi.org/10.5194/acp-17-12845-2017>, 2017.
- Mironov, D., Ritter, B., Schulz, J.-P., Buchhold, M., Lange, M., and MacHulskaaya, E.: Parameterisation of sea and lake ice in numerical weather prediction models of the German Weather Service, *Tellus A: Dynamic Meteorology and Oceanography*, 64, 17 330, <https://doi.org/10.3402/tellusa.v64i0.17330>, 2012.
- Mlawer, E. J., Taubman, S. J., Brown, P. D., Iacono, M. J., and Clough, S. A.: Radiative transfer for inhomogeneous atmospheres: RRTM, a validated correlated-k model for the longwave, *Journal of Geophysical Research: Atmospheres*, 102, 16 663–16 682, <https://doi.org/10.1029/97JD00237>, 1997.
- Morrison, H. and Pinto, J. O.: Mesoscale Modeling of Springtime Arctic Mixed-Phase Stratiform Clouds Using a New Two-Moment Bulk Microphysics Scheme, *Journal of the Atmospheric Sciences*, 62, 3683–3704, <https://doi.org/10.1175/JAS3564.1>, 2005.
- Neggers, R. A. J., Chylik, J., Egerer, U., Griesche, H., Schemann, V., Seifert, P., Siebert, H., and Macke, A.: Local and Remote Controls on Arctic Mixed-Layer Evolution, *Journal of Advances in Modeling Earth Systems*, 11, 2214–2237, <https://doi.org/10.1029/2019MS001671>, 2019.
- Petty, G. W. and Huang, W.: The Modified Gamma Size Distribution Applied to Inhomogeneous and Nonspherical Particles: Key Relationships and Conversions, *Journal of the Atmospheric Sciences*, 68, 1460–1473, <https://doi.org/10.1175/2011JAS3645.1>, 2011.
- Phillips, V. T. J., DeMott, P. J., and Andronache, C.: An Empirical Parameterization of Heterogeneous Ice Nucleation for Multiple Chemical Species of Aerosol, *Journal of the Atmospheric Sciences*, 65, 2757–2783, <https://doi.org/10.1175/2007JAS2546.1>, 2008.
- Pinto, J. O.: Autumnal Mixed-Phase Cloudy Boundary Layers in the Arctic, *Journal of the Atmospheric Sciences*, 55, 2016–2038, [https://doi.org/10.1175/1520-0469\(1998\)055<2016:AMPCBL>2.0.CO;2](https://doi.org/10.1175/1520-0469(1998)055<2016:AMPCBL>2.0.CO;2), 1998.
- Pithan, F. and Mauritsen, T.: Arctic amplification dominated by temperature feedbacks in contemporary climate models, *Nature Geoscience*, 7, 181–184, <https://doi.org/10.1038/ngeo2071>, 2014.
- Pithan, F., Medeiros, B., and Mauritsen, T.: Mixed-phase clouds cause climate model biases in Arctic wintertime temperature inversions, *Climate Dynamics*, 43, 289–303, <https://doi.org/10.1007/s00382-013-1964-9>, 2014.
- Rauber, R. M. and Tokay, A.: An Explanation for the Existence of Supercooled Water at the Top of Cold Clouds, *Journal of the Atmospheric Sciences*, 48, 1005–1023, [https://doi.org/10.1175/1520-0469\(1991\)048<1005:AEFTEO>2.0.CO;2](https://doi.org/10.1175/1520-0469(1991)048<1005:AEFTEO>2.0.CO;2), 1991.
- Ruiz-Donoso, E., Ehrlich, A., Schäfer, M., Jäkel, E., Schemann, V., Crewell, S., Mech, M., Kulla, B. S., Kliesch, L.-L., Neuber, R., and Wendisch, M.: Small-scale structure of thermodynamic phase in Arctic mixed-phase clouds observed by airborne remote sensing during a cold air outbreak and a warm air advection event, *Atmospheric Chemistry and Physics*, 20, 5487–5511, <https://doi.org/10.5194/acp-20-5487-2020>, 2020.
- Schäfer, M., Loewe, K., Ehrlich, A., Hoose, C., and Wendisch, M.: Simulated and observed horizontal inhomogeneities of optical thickness of Arctic stratus, *Atmospheric Chemistry and Physics*, 18, 13 115–13 133, <https://doi.org/10.5194/acp-18-13115-2018>, 2018.



- Schemann, V. and Ebell, K.: Simulation of mixed-phase clouds with the ICON large-eddy model in the complex Arctic environment around Ny-Ålesund, *Atmospheric Chemistry and Physics*, 20, 475–485, <https://doi.org/10.5194/acp-20-475-2020>, 2020.
- Schnaiter, M. and Järvinen, E.: SID-3 1 Hz size distribution of cloud particles during the ACLOUD campaign in 2017, <https://doi.org/10.1594/PANGAEA.900261>, 2019.
- 650 Schnaiter, M., Järvinen, E., Vochezer, P., Abdelmonem, A., Wagner, R., Jourdan, O., Mioche, G., Shcherbakov, V. N., Schmitt, C. G., Tricoli, U., Ulanowski, Z., and Heymsfield, A. J.: Cloud chamber experiments on the origin of ice crystal complexity in cirrus clouds, *Atmospheric Chemistry and Physics*, 16, 5091–5110, <https://doi.org/10.5194/acp-16-5091-2016>, 2016.
- Schneider, T., Teixeira, J., Bretherton, C. S., Brient, F., Pressel, K. G., Schär, C., and Siebesma, A. P.: Climate goals and computing the future of clouds, *Nature Climate Change*, 7, 3–5, <https://doi.org/10.1038/nclimate3190>, 2017.
- 655 Screen, J. A. and Simmonds, I.: The central role of diminishing sea ice in recent Arctic temperature amplification., *Nature*, 464, 1334–1337, <https://doi.org/10.1038/nature09051>, 2010.
- Seifert, A. and Beheng, K. D.: A two-moment cloud microphysics parameterization for mixed-phase clouds. Part 1: Model description, *Meteorology and Atmospheric Physics*, 92, 45–66, <https://doi.org/10.1007/s00703-005-0112-4>, 2006.
- Serreze, M. C. and Barry, R. G.: Processes and impacts of Arctic amplification: A research synthesis, *Global and Planetary Change*, 77, 660 85–96, <https://doi.org/10.1016/j.gloplacha.2011.03.004>, 2011.
- Shupe, M. D. and Intrieri, J. M.: Cloud radiative forcing of the Arctic surface: The influence of cloud properties, surface albedo, and solar zenith angle, *Journal of Climate*, 17, 616–628, [https://doi.org/10.1175/1520-0442\(2004\)017<0616:CRFOTA>2.0.CO;2](https://doi.org/10.1175/1520-0442(2004)017<0616:CRFOTA>2.0.CO;2), 2004.
- Shupe, M. D., Kollias, P., Persson, P. O. G., and McFarquhar, G. M.: Vertical Motions in Arctic Mixed-Phase Stratiform Clouds, *Journal of the Atmospheric Sciences*, 65, 1304–1322, <https://doi.org/10.1175/2007JAS2479.1>, 2008.
- 665 Sotiropoulou, G., Tjernström, M., Savre, J., Ekman, A. M. L., Hartung, K., and Sedlar, J.: Large-eddy simulation of a warm-air advection episode in the summer Arctic, *Quarterly Journal of the Royal Meteorological Society*, 144, 2449–2462, <https://doi.org/10.1002/qj.3316>, 2018.
- Stapf, J., Ehrlich, A., Jäkel, E., Lüpkes, C., and Wendisch, M.: Reassessment of the common concept to derive the surface cloud radiative forcing in the Arctic: Consideration of surface albedo-cloud interactions, *Atmospheric Chemistry and Physics Discussions*, 670 <https://doi.org/10.5194/acp-2019-534>, 2019a.
- Stapf, J., Ehrlich, A., Jäkel, E., and Wendisch, M.: Aircraft measurements of broadband irradiance during the ACLOUD campaign in 2017, <https://doi.org/10.1594/PANGAEA.900442>, 2019b.
- Stevens, B., Satoh, M., Auger, L., Biercamp, J., Bretherton, C. S., Chen, X., Düben, P., Judt, F., Khairoutdinov, M., Klocke, D., Kodama, C., Kornblüeh, L., Lin, S.-J., Neumann, P., Putman, W. M., Röber, N., Shibuya, R., Vanniere, B., Vidale, P. L., Wedi, N., and Zhou, 675 L.: DYAMOND: the DYnamics of the Atmospheric general circulation Modeled On Non-hydrostatic Domains, *Progress in Earth and Planetary Science*, 6, 61, <https://doi.org/10.1186/s40645-019-0304-z>, 2019.
- Stevens, B., Acquistapace, C., Hansen, A., Heinze, R., Klinger, C., Klocke, D., Rybka, H., Schubotz, W., Windmiller, J., Adamidis, P., Arka, I., Barlakas, V., Biercamp, J., Brueck, M., Brune, S., Buehler, S. A., Burkhardt, U., Cioni, G., Costa-Surós, M., Crewell, S., Crüger, T., Deneke, H., Friederichs, P., Henken, C. C., Hohenegger, C., Jacob, M., Jakub, F., Kalthoff, N., Köhler, M., van Laar, T. W., Li, P., Löhnert, 680 U., Macke, A., Madenach, N., Mayer, B., Nam, C., Naumann, A. K., Peters, K., Poll, S., Quaas, J., Röber, N., Rochetin, N., Scheck, L., Schemann, V., Schnitt, S., Seifert, A., Senf, F., Shapkalijevski, M., Simmer, C., Singh, S., Sourdeval, O., Spickermann, D., Strandgren, J., Tessiot, O., Vercauteren, N., Vial, J., Voigt, A., and Zängl, G.: The Added Value of Large-Eddy and Storm-Resolving Models for Simulating Clouds and Precipitation, *Journal of the Meteorological Society of Japan. Ser. II*, <https://doi.org/10.2151/jmsj.2020-021>, 2020.



- 685 Stramler, K., Del Genio, A. D., and Rossow, W. B.: Synoptically driven Arctic winter states, *Journal of Climate*, 24, 1747–1762,
<https://doi.org/10.1175/2010JCLI3817.1>, 2011.
- Tiedtke, M.: A Comprehensive Mass Flux Scheme for Cumulus Parameterization in Large-Scale Models, *Monthly Weather Review*, 117,
1779–1800, [https://doi.org/10.1175/1520-0493\(1989\)117<1779:ACMFSF>2.0.CO;2](https://doi.org/10.1175/1520-0493(1989)117<1779:ACMFSF>2.0.CO;2), 1989.
- 690 Tonttila, J., O'Connor, E. J., Niemelä, S., Räisänen, P., and Järvinen, H.: Cloud base vertical velocity statistics: A comparison be-
tween an atmospheric mesoscale model and remote sensing observations, *Atmospheric Chemistry and Physics*, 11, 9207–9218,
<https://doi.org/10.5194/acp-11-9207-2011>, 2011.
- Twomey, S.: The Influence of Pollution on the Shortwave Albedo of Clouds, *Journal of the Atmospheric Sciences*, 34, 1149–1152,
[https://doi.org/10.1175/1520-0469\(1977\)034<1149:TIOPO>2.0.CO;2](https://doi.org/10.1175/1520-0469(1977)034<1149:TIOPO>2.0.CO;2), 1977.
- 700 Wendisch, M., Macke, A., Ehrlich, A., Lüpkes, C., Mech, M., Chechin, D., Dethloff, K., Velasco, C. B., Bozem, H., Brückner, M., Clemen,
H.-C., Crewell, S., Donth, T., Dupuy, R., Ebell, K., Egerer, U., Engelmann, R., Engler, C., Eppers, O., Gehrmann, M., Gong, X.,
Gottschalk, M., Gourbeyre, C., Griesche, H., Hartmann, J., Hartmann, M., Heinold, B., Herber, A., Herrmann, H., Heygster, G., Hoor, P.,
Jafariserajehlou, S., Jäkel, E., Järvinen, E., Jourdan, O., Kästner, U., Kecorius, S., Knudsen, E. M., Köllner, F., Kretzschmar, J., Lelli, L.,
Leroy, D., Maturilli, M., Mei, L., Mertes, S., Mioche, G., Neuber, R., Nicolaus, M., Nomokonova, T., Notholt, J., Palm, M., van Pinx-
teren, M., Quaas, J., Richter, P., Ruiz-Donoso, E., Schäfer, M., Schmieder, K., Schnaiter, M., Schneider, J., Schwarzenböck, A., Seifert, P.,
Shupe, M. D., Siebert, H., Spreen, G., Stapf, J., Stratmann, F., Vogl, T., Welti, A., Wex, H., Wiedensohler, A., Zanatta, M., and Zeppenfeld,
S.: The Arctic Cloud Puzzle: Using ALOUD/PASCAL Multiplatform Observations to Unravel the Role of Clouds and Aerosol Particles
in Arctic Amplification, *Bulletin of the American Meteorological Society*, 100, 841–871, <https://doi.org/10.1175/BAMS-D-18-0072.1>,
2019.
- Wesche, C., Steinhage, D., and Nixdorf, U.: Polar aircraft Polar 5 and Polar 6 operated by the Alfred Wegener Institute, *Journal of large-scale
research facilities JLSRF*, 2, A87, <https://doi.org/10.17815/jlsrf-2-153>, 2016.
- 705 Zängl, G., Reinert, D., Rípodas, P., and Baldauf, M.: The ICON (ICOsahedral Non-hydrostatic) modelling framework of DWD and
MPI-M: Description of the non-hydrostatic dynamical core, *Quarterly Journal of the Royal Meteorological Society*, 141, 563–579,
<https://doi.org/10.1002/qj.2378>, 2015.